JOURNAL OF COMPUTATIONAL PHYSICS 104, 150–161 (1993)

Lagrangian Solution of Supersonic Real Gas Flows

CHING-YUEN LOH

AND

MENG-SING LIOU

International Fluid Mechanics Division, NASA Lewis Research Center, Cleveland, Ohio 44135

Received October 17, 1991; revised April 28, 1992

This paper details the procedure of the real gas Riemann solution in the Lagrangian approach originally proposed by Loh and Hui for perfect gases. The extension to real gases is nontrivial and requires substantial development of an exact real-gas Riemann solver for the Lagrangian form of conservation laws. The first-order Gudonov scheme is enhanced for accuracy by adding limited anti-diffusive terms according to Sweby. Extensive calculations were made to test the accuracy and robustness of the present real gas Lagrangian approach, including complex wave interactions of different types. The accuracy for capturing 2D oblique waves and slip line is clearly demonstrated. In addition, we also show the real gas effect in a generic engine nozzle.

1. INTRODUCTION

Enormous progress have been made in the past decades in computational fluid dynamics in terms of discretization and solution techniques. In the 1980s, we have witnessed exhaustive exploration of upwind, monotone schemes, notably exact Riemann solver by Gudonov [1] and various approximate Riemann solvers [2–5]. However, these developments are nearly restricted to the Eulerian description of the conservation laws vs the Lagrangian description. The notion of using the Lagrangian approach is not new. Particularly noteworthy is the work carried out at Los Alamos and Lawrence Livermore Laboratories during the 1950s and 1960s. In the Lagrangian approach, the computational grid (fluid pocket) is embedded in the fluid and distorts with the fluid motion. The most severe limitation is its inability to cope with the flow with large distortion since the grid becomes tangled and disordered [6]. Thus, some combinations of both the Eulerian and Lagrangian approaches were attempted, such as the arbitrary Lagrangian–Eulerian (ALE) method, to allow much more freedom for accommodating fluid distortion. Generally, a continuous rezoning procedure is needed to maintain the grid regularity as far as possible. This procedure requires the specification of grid displacement during the evolution of fluid. Unfortunately, loss of accuracy in the solution is also accompanied via the continuous geometrical interpolation. As a result, since the late 1960s the Eulerian approach has been favored for its grid regularity and ease of controlling grid distortion even if the fluid is greatly distorted. However, the very virtue of the Lagrangian approach to follow the fluid movement, specifically the trajectory of a slip line, is compromised in the Eulerian approach through the mixing of mass (fluid) between neighboring grid points, without any distinction of slip boundary and grid boundary. Thus, the Eulerian approach comes at the expense of precise slip line definition. Recently, Loh and Hui [7] have successfully demonstrated the capability of a new Lagrangian formulation that eliminates the step of remapping. Indeed, in the case of supersonic flows, the computational grid is automatically generated following the streamlines. Grid of severe distortion caused by complex strong wave interactions or geometrical boundary can also be easily tolerated.

With the renewed interest in high-speed flight, the real gas and nonequilibrium effects must be taken into account in the analysis of flow in this regime. Several extensions of the above-mentioned upwind schemes have been made possible in the Eulerian approach (see, e.g., [8, 9]). Although there is no conceptual difficulty in the extension, however, some generalization must be made. The procedure certainly becomes more involved. In the present Lagrangian approach, the real gas Riemann solver is a basic building block for the wave structure at the interface straddling two neighboring fluid volumes. The exact solution of the Riemann problem, instead of the approximate solution, is sought in our study.

In Section 2 we present the Lagrangian form of conservative laws and the equation of state (EOS) used for the equilibrium air. The first-order Godunov scheme is enhanced to a high-resolution TVD scheme. In Section 3,

0021-9991/93 $5.00

we describe the exact Riemann solution of Lagrangian formulation for real gases. Finally, several test problems are given in Section 4.

2. THE LAGRANGIAN CONSERVATION FORM FOR REAL GAS AND APPLICATION OF HIGH RESOLUTION TVD SCHEME

Based on the new Lagrangian formulation of Hui and Van Roessel [10], Loh and Hui [7] used the stream function ξ and the "Lagrangian time" τ as the independent variables (Fig. 1) in their computation for 2D steady supersonic flow. In this case, the Lagrangian time is indeed also interpreted as the physical time assigned for each fluid particle. The conservation form based on this variable transformation are given as

$$\frac{\partial \mathbf{E}}{\partial \tau}+\frac{\partial \mathbf{F}}{\partial \xi}=0 \tag{1}$$

with

$$\mathbf{E}=\begin{pmatrix} e_1 \\ e_2 \\ e_3 \\ e_4 \\ e_5 \\ e_6 \end{pmatrix}=\begin{pmatrix} K \\ H \\ Ku+pV \\ Kv-pU \\ U \\ V \end{pmatrix}, \qquad \mathbf{F}=\begin{pmatrix} 0 \\ 0 \\ -pv \\ pu \\ -u \\ -v \end{pmatrix},$$

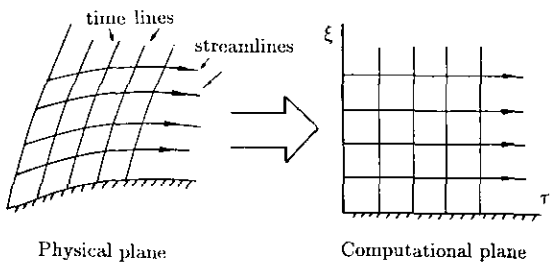

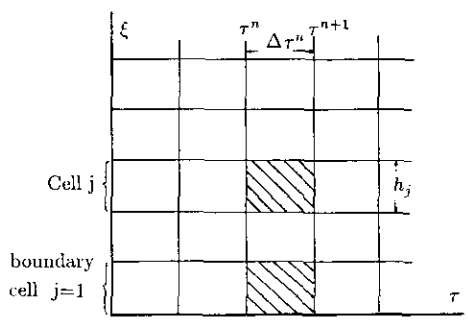

FIG. 1. Computational domain and mesh.

where, as usual, u, v, p, and ρ are respectively Cartesian velocity components, pressure, and density of the fluid;

$$U=\frac{\partial x}{\partial \xi}, \qquad V=\frac{\partial y}{\partial \xi},$$

are the geometrical quantities representing fluid particle deformation during marching forward. The variable

$$K=\rho(uV-vU) \tag{2}$$

is the mass flux and H is the specific total enthalpy,

$$H=(u^2+v^2)/2+h(p,\rho), \tag{3}$$

where h is the enthalpy. The first four equations in (1) represent the physical conservation laws of mass, energy, and momentum, respectively, while the last two arise from the compatibility condition between the τ-derivatives and the ξ-derivatives, representing the deformation of a fluid particle.

For steady flow at supersonic speed (1) holds for any gases. For real gases, the equation of state (EOS) is more complicated, but any pair of independent thermodynamic variables are sufficient to describe the state. In our formulation, we choose

$$h=h(p,\rho)=e(p,\rho)+p/\rho.$$

The internal energy e is a prescribed function of p and ρ. The one we use throughout the present paper is Tannehill's equation of state for air [11], which is based on the table lookup interpolation, with a reported error of 4%.

The numerical solution of (1) by Godunov scheme and the consequent high resolution TVD scheme with Sweby's flux limiter has been described in detail in [12, 13], respectively. Here, to avoid repetition, we shall only give an outline of the procedure, while pointing out the differences and describing in detail the additional procedures required for real gases.

In order to solve the initial boundary value problem of the hyperbolic system (1), the computational domain (Fig. 1) is divided by streamlines $0=\xi_0<\xi_1<\xi_2<\cdots<\xi_N$, into N cells of size $h_j=\xi_j-\xi_{j-1}$, $j=1, 2, ..., N$. Initially at time $\tau=\tau_0$, the flow variables $\mathbf{Q}=(p, \rho, u, v)^{\mathrm{T}}$ and the geometrical variables (U, V) are given along the initial time line. The solution is to be evaluated for every cell $j=1, 2, ..., N$, at time $\tau=\tau_1, \tau_2, ...$

For $\tau=\tau_n$ the flow variables $\mathbf{Q}$ and (U, V) are assumed given and constant within each cell j, denoted as $\mathbf{Q}_j$, U_j, and V_j. A sequence of Riemann problems with initial data

$$\mathbf{Q}=\begin{cases}\mathbf{Q}_{j+1}, & \xi>\xi_j, \\ \mathbf{Q}_j, & \xi<\xi_j,\end{cases} \qquad j=1, 2, ..., N-1, \tag{4}$$

are solved to determine the interaction between flows in adjacent cells and subsequently the fluxes $\mathbf{F}_{j+1/2}^{n+1/2}$ at the cell interfaces. The solution procedure for real gas Riemann problem is substantially different from the one for perfect gas, the details are given in Section 3. Then the divergence theorem is applied to update $\mathbf{E}_j^n$ to $\mathbf{E}_j^{n+1}$,

$$\mathbf{E}_j^{n+1} = \mathbf{E}_j^n - \lambda(\mathbf{F}_{j+1/2}^{n+1/2} - \mathbf{F}_{j-1/2}^{n+1/2}), \tag{5}$$

where $\lambda = \Delta\tau_n/h_j$ and $\Delta\tau_n = \tau_{n+1} - \tau_n$ is the time step size.

To enhance the numerical result, we use Sweby's formula [12] to extend the above first-order Godunov scheme to a high resolution TVD scheme in the same manner as in [13],

$$\begin{aligned}\mathbf{E}_j^{n+1} = \mathbf{E}_j^n &- \lambda\Delta_- \mathbf{F}_{j+1/2}^{n+1/2} \\ &- \lambda\Delta_- \{\phi(r_j^+)\,\alpha_{j+1/2}^+ [\Delta\mathbf{F}_{j+1/2}]^+ \\ &- \phi(r_{j+1}^-)\,\alpha_{j+1/2}^- [\Delta\mathbf{F}_{j+1/2}]^-\},\end{aligned} \tag{6}$$

where

$$\begin{aligned}\Delta_- g_{j+1/2} &= g_{j+1/2} - g_{j-1/2}, \\ [\Delta\mathbf{F}_{j+1/2}]^+ &= \mathbf{F}(\mathbf{Q}_{j+1}^n) - \mathbf{F}_{j+1/2}^{n+1/2}, \\ [\Delta\mathbf{F}_{j+1/2}]^- &= \mathbf{F}_{j+1/2}^{n+1/2} - \mathbf{F}(\mathbf{Q}_j^n), \\ \alpha_{j+1/2}^{\pm} &= \tfrac{1}{2}[1 \mp \nu_{j+1/2}^{\pm}], \\ \nu_{j+1/2}^{\pm} &= \frac{\lambda[\Delta(f_i)_{j+1/2}]^{\pm}}{[(e_i)_{j+1}^n - (e_i)_j^n]}, \\ r_j^{\pm} &= \left[\frac{\alpha_{j-1/2}^{\pm}(\Delta(f_i)_{j-1/2})^{\pm}}{\alpha_{j+1/2}^{\pm}(\Delta(f_i)_{j+1/2})^{\pm}}\right]^{\pm 1} \\ &\qquad (i = 3, 4, 5, 6).\end{aligned} \tag{7, 8}$$

We note that since $e_1 = K$, $e_2 = H$ are constant for all τ along a streamline, the numerical procedure needs to be applied to only four equations (same number as in the Eulerian case), namely, equations for e_3, e_4, e_5, and e_6. The Van Leer limiter function,

$$\phi(r) = \begin{cases} 0, & r < 0, \\ \dfrac{r}{r+1}, & r > 0, \end{cases} \tag{9}$$

is employed throughout this paper since it was found in [13] that there is no substantial difference in the numerical results between using different limiter functions. Moreover, discussion of the choice of the limiter is beyond the scope of the present paper.

In real gas computation, the decoding procedure to recover $\mathbf{Q} = (p, \rho, u, v)^T$, and (U, V) from $\mathbf{E} = \mathbf{E}_j^{n+1}$ is more complicated than that for perfect gas. The following gives the detailed description of the decoding.

First, (U, V) are obtained directly from e_5 and e_6:

$$U = e_5$$
$$V = e_6.$$

Then, if p is known, u, v, and ρ are easily computed:

$$u = \frac{e_3 - pe_6}{e_1}, \qquad v = \frac{e_4 + pe_5}{e_1}, \tag{10}$$

$$\rho = \frac{e_1^2}{[(e_3e_6 - e_4e_5) - p(e_5^2 + e_6^2)]}. \tag{11}$$

In order to solve for p, by substituting (10), (11) into (3) we have

$$\begin{aligned}f(p, \rho) = (e_3^2 + e_4^2) - (e_5^2 + e_6^2)\,p^2 \\ + 2e_1^2 e(p, \rho) - 2e_2e_1^2 = 0,\end{aligned} \tag{12}$$

where $e(p, \rho)$ is the given EOS and is an awfully complex function for real gas. In the present paper, EOS are obtained from Tannehill's subroutines [11]. In the case of perfect gas, (11) and (12) are combined to yield a single quadratic equation for p; one of the two roots can be ruled out for it gives nonphysical solution. On the other hand, the real gas case requires a simultaneous solution of the coupled nonlinear system of (11) and (12) for which we employ the Newton iterative procedure. Due to the presence of inflection points in Tannehill's equations of state, which is associated with the change of internal degrees of freedom of components of the air, the Newton iteration fails to converge and leads to a limit cycle (Fig. 2). We remedy this by introducing a bisection approximation,

$$\hat{x} = \tfrac{1}{2}(x^{(n)} + x^{(n+1)}),$$

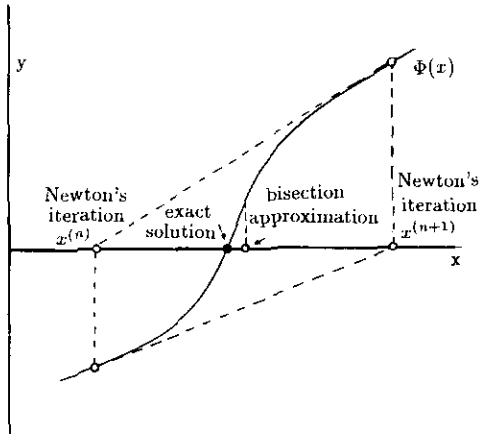

FIG. 2. Possible failure of Newton's iteration around an inflection point in the solution of $\Phi(x) = 0$ and the bisection method.

where $x^{(n)}$ and $x^{(n+1)}$ are two successive Newton's iterations with opposite signs in their corresponding object function values. Using the bisection approximation guarantees convergence of the iterative procedure at the price of slightly reduced rate of convergence in the case the original Newton procedure converges. Such a modified Newton iterative procedure is used not only in the decoding process but also in the solution of Riemann problem as well. Details will be given in the next section.

The marching computation at the new time line $\tau = \tau_{n+1}$ is complete with the evaluation of the new cell locations (x_j^{n+1}, y_j^{n+1}), $j = 1, 2, ..., N$. This is done by simple integration along the streamlines:

$$x_j^{n+1} = x_j^n + \tfrac{1}{2}\Delta\tau_n (u_j^n + u_j^{n+1}),$$
$$y_j^{n+1} = y_j^n + \tfrac{1}{2}\Delta\tau_n (v_j^n + v_j^{n+1}). \tag{13}$$

A note of caution about determining the marching step is warranted at this point. In addition to the usual Courant condition for stability, there is another consideration concerning the interactions (or Riemann problem) between two adjacent fluid particles which are separated by a strong slip line (also a streamline). Because of the difference in flow speed, they will gradually lose physical contact and eventually become separated, thereby rendering the Riemann solution inappropriate. A simple remedy is to adjust the time step $\Delta\tau$ of the faster-moving cells so that the two cells across the strong slip line can march forward in the same distance $(\sqrt{u^2+v^2}\,\Delta\tau)$ and thus keep physical contact all the time.

If there is a solid boundary, the boundary Riemann solver is employed. Details about the boundary Riemann solver are described in the next section. If there is any slope discontinuity at the solid boundary, the same special treatments as described in [4] are applied to minimize numerical errors. As a matter of fact, these special treatments amount to apply a local exact solution at the sudden turns of the solid body surface.

3. SOLUTION OF THE REAL GAS RIEMANN PROBLEM

As a building block, the Riemann problem and its solution play an important role in the Godunov-type schemes in the numerical solution of invicid compressible real gas flow problems. In this section, we consider the real gas Riemann problem and its solution. As we have mentioned before, our purpose is to develop an "exact" numerical method for computing real gas flow that is accurate to the extent warranted by the equations of state, i.e., by the table lookup interpolation. In this study, we choose not to make mathematical approximations in the solution of the real gas Riemann problem; and the numerical approximations are made as accurate as possible. In other words, we seek the exact Riemann solution in the present calculations. In principle, the solution procedure is similar to the one in [7]. However, due to the real gas effect, the detailed steps are different.

The Riemann problem for the two-dimensional steady supersonic real gas flow is the initial value problem with the constant data,

$$\mathbf{Q} = \begin{cases} \mathbf{Q}_T, & \xi > \xi_j, \\ \mathbf{Q}_B, & \xi < \xi_j, \end{cases} \tag{14}$$

as initial condition at $\tau = 0$ for the flow state $\mathbf{Q} = (p, \rho, u, v)^T$ and with the equation of state

$$e = e(p, \rho), \tag{15}$$

where the subscripts T and B denote top and bottom states (Fig. 3), which are counterparts to the left and right states in one-dimensional unsteady flow. The equation of state (EOS) (15) is prescribed as a given function.

The solution of the Riemann problem is self-similar in the variable ξ/τ (or τ/ξ) and similar to the perfect gas Riemann problem, consists of three types of elementary waves, namely, the oblique shock (+), the Prandtl–Meyer expansion (−), and the slip line (0), as illustrated in Fig. 3.

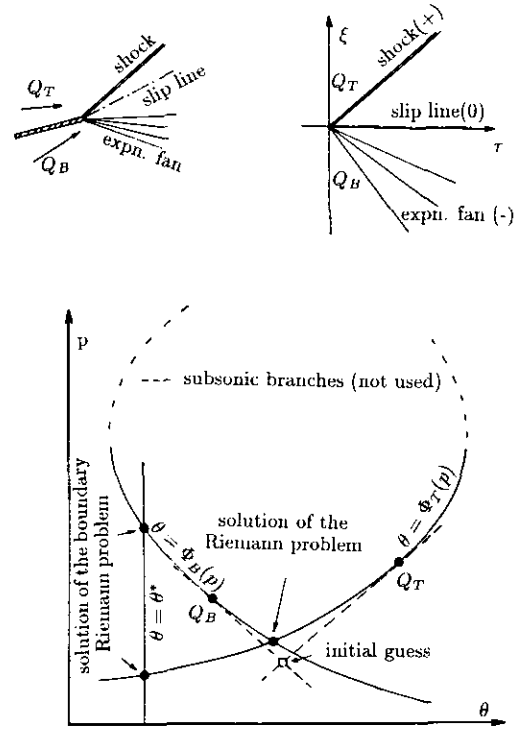

FIG. 3. Real gas Riemann problem and its solution.

We will consider these elementary waves separately. Let $\mathbf{Q_0}$ and $\mathbf{Q}$ be the states across one of the above $+$, $-$, and 0 elementary waves. Then there are three cases:

(a) The wave is a slip line. In this case, we simply have

$$\begin{aligned} p &= p_0 = p^*, \\ \theta &= \tan^{-1}(v/u) = \tan^{-1}(v_0/u_0) = \theta^*, \end{aligned} \tag{16}$$

where p^* and θ^* are respectively the pressure and flow inclination angle across the slip line. However, the density and velocity may jump abruptly across the slip line.

(b) The wave is an oblique shock. In this case, we start with the following oblique shock relations and EOS,

$$\rho_0/\rho = 1 - \frac{p - p_0}{\rho_0 q_0^2 \sin^2\beta}, \tag{17}$$

$$\tan\delta = \frac{(\rho - \rho_0)\tan\beta}{\rho + \rho_0 \tan^2\beta}, \tag{18}$$

$$q_0^2 \sin^2\beta = \frac{p^2 - p_0^2}{2\rho_0^2(e - e_0)}, \tag{19}$$

$$e = e(p, \rho), \qquad (e_0 = e(p_0, \rho_0)), \tag{20}$$

where $q = \sqrt{u^2 + v^2}$ ($q_0 = \sqrt{u_0^2 + v_0^2}$), β is the shock angle, and $\delta = \Delta\theta$ is the flow deflection angle.

By first substituting (20) into (19) and then (19) into (17), we find an implicit relation between p and ρ, viz. the Rankine–Hugoniot relation:

$$\rho_0/\rho = 1 - 2\rho_0 \frac{e(p, \rho) - e(p_0, \rho_0)}{p + p_0}. \tag{21}$$

If p is known, ρ can be worked out from (21) by the modified Newton procedure described in the previous section:

$$\rho = \rho(p). \tag{22}$$

The shock angle is evaluated through

$$\beta = \sin^{-1}\left[\sqrt{\frac{(p - p_0)\rho}{(\rho - \rho_0)\rho_0}} \Big/ q_0\right]. \tag{23}$$

From (23), (22), and (18), we have the relation between flow deflection angle δ and pressure p:

$$\delta = \delta(p) = \tan^{-1}\left[\frac{(\rho - \rho_0)\tan\beta}{\rho + \rho_0 \tan^2\beta}\right]. \tag{24}$$

The flow inclination then is

$$\theta = \Phi_{\mathrm{T}}(p) = \theta_0 + \delta \tag{25a}$$

for the flow on the top; and

$$\theta = \Phi_{\mathrm{B}}(p) = \theta_0 - \delta \tag{25b}$$

for the flow on the bottom.

(c) The wave is a Prandtl–Meyer expansion. In this case, we use the isentropic relations,

$$T\,ds = de + p\,d(1/\rho) = 0, \tag{26}$$

where s is the entropy and T the temperature. Equation (26) leads to the expression for speed of sound,

$$a^2 = (dp/d\rho)_s = \frac{p/\rho^2 - e_\rho}{e_p}, \tag{27}$$

where

$$e_p = \frac{\partial e}{\partial p}, \qquad e_\rho = \frac{\partial e}{\partial \rho}.$$

Equation (27) may be regarded as an ordinary differential equation for ρ with initial condition $\rho = \rho_0$:

$$\frac{d\rho}{dp} = 1/a^2 = \frac{e_p}{p/\rho^2 - e_\rho}. \tag{28}$$

In practice, we scale p by using $\ln(p)$ as the variable to reduce the stiffness of the ODE and a fourth-order Runge–Kutta method with adaptive step size is employed to solve for ρ. Once p and ρ are known, $q^2 = u^2 + v^2$ is easily available from the total enthalpy H,

$$q^2 = 2(H - e(p, \rho) - p/\rho), \tag{29}$$

and the local Mach number M follows directly:

$$M^2 = q^2/a^2 = \frac{2(H - e(p, \rho) - p/\rho)\,e_p}{p/\rho^2 - e_\rho}. \tag{30}$$

From the isentropic condition and $H = \text{const}$, we have

$$dh = dp/\rho, \qquad dq = dp/\rho q.$$

The local flow deflection angle $d\theta$ is then

$$d\theta = \mp \frac{dq}{q}\sqrt{M^2 - 1} = \pm \frac{\sqrt{M^2 - 1}}{\rho q^2}\,dp. \tag{31}$$

Now the flow inclination becomes

$$\theta = \Phi_{\mathrm{T}}(p) = \theta_0 + \int_{p_0}^{p} \frac{\sqrt{M^2 - 1}}{\rho q^2}\,dp \tag{32a}$$

for the flow on the top and

$$\theta = \Phi_B(p) = \theta_0 - \int_{p_0}^{p} \frac{\sqrt{M^2-1}}{\rho q^2}\, dp \tag{32b}$$

for the flow on the bottom. The integrals (32) are evaluated numerically by Simpson's rule. They play a role in the formulation similar to the Prandtl–Meyer function in perfect gas.

Therefore, through any state $\mathbf{Q}_0$, with p as parameter, there are two families of state connecting to $\mathbf{Q}_0$, namely, the compression states ($p \geqslant p_0$) and the expansion states ($p \leqslant p_0$). As in perfect gas, the two families join smoothly at $\mathbf{Q}_0$ and can be regarded as a single family. This makes it possible to apply Newton's iterative procedure in the solution of the Riemann problem. We now illustrate the solution details.

(i) In the p-θ plane (Fig. 3), there are two curves passing through the states $\mathbf{Q}_0 = \mathbf{Q}_T$ and $\mathbf{Q}_0 = \mathbf{Q}_B$; they are defined as

$$\theta = \Phi_T(p) = \begin{cases} \theta_0 + \displaystyle\int_{p_0}^{p} \frac{\sqrt{M^2-1}}{\rho q^2}\, dp, \\ \qquad p \leqslant p_0 \\ \theta_0 + \tan^{-1}\left[\dfrac{(\rho-\rho_0)\tan\beta}{\rho + \rho_0 \tan^2\beta}\right], \\ \qquad p > p_0; \end{cases} \tag{33a}$$

and

$$\theta = \Phi_B(p) = \begin{cases} \theta_0 - \displaystyle\int_{p_0}^{p} \frac{\sqrt{M^2-1}}{\rho q^2}\, dp, \\ \qquad p \leqslant p_0 \\ \theta_0 - \tan^{-1}\left[\dfrac{(\rho-\rho_0)\tan\beta}{\rho + \rho_0 \tan^2\beta}\right], \\ \qquad p > p_0. \end{cases} \tag{33b}$$

These curves are sketched in Fig. 3.

(ii) the modified Newton procedure as described in the previous section is then employed to find the intersect (p^*, θ^*) of the two curves. The object function in the Newton procedure is

$$f(p) = \Phi_T(p) - \Phi_B(p) \tag{34}$$

and the intersect of the tangent lines passing through $\mathbf{Q}_T$ and $\mathbf{Q}_B$ is used as an initial guess to the solution. In practice we use numerical derivative to replace the analytical ones. Usually it takes two to four iterations to converge to a tolerance less than 10^{-6}. However, the evaluation of Φ_T and Φ_B takes considerably more CPU time than in the perfect gas case, which is the price one has to pay for an accurate real gas result.

(iii) With the slip line values (p^*, θ^*) calculated, we calculate ρ using the appropriate equation ((22) for compression state and the ODE; (28) for expansion) and then calculate q using (29). Velocity components are easily obtained by

$$u = q\cos\theta^*, \qquad v = q\sin\theta^*. \tag{35}$$

At the solid boundary, the flow inclination condition is imposed and one of the curves, say, $\theta = \Phi_B(p)$ degenerates to a straight line $\theta = \theta^* = \text{const.}$ parallel to the p axis (Fig. 3). In [7], this particular problem is termed "boundary Riemann problem." The solution of a boundary Riemann problem is similar to the above procedure except using a different object function:

$$f(p) = \Phi_T(p) - \theta^*$$

or

$$f(p) = \Phi_B(p) - \theta^*.$$

4. TEST PROBLEMS

The Lagrangian method for real gas is tested in several examples for accuracy and robustness. The numerical results are compared with the available exact solutions. These examples include features of the basic elementary waves, namely, the oblique shocks (+), the slip lines (0), and the Prandtl–Meyer expansions (−). In some examples, we present the real gas solution as well as the perfect gas solution for comparison. Throughout the examples, the MKS unit system is used. However, for convenience, the unit for pressure is atmospheric pressure (atm), and the unit for temperature is K.

The first example is a pure initial value problem, namely a Riemann problem. The top and bottom states are shown in Fig. 4. We use 100 uniform cells with $h_j = 0.01$ and the EOS in this example is simply the one for a perfect gas, i.e., $e = (1/(\gamma-1))\, p/\rho$; $\gamma = 1.4$. At a lower temperature such as in this problem, Tannehill's EOS is identical to that of a perfect gas. From Fig. 4 it is seen that the numerical results agree well with the perfect gas exact solution (solid lines) and the slip line and shock are resolved with two and three points, respectively.

We then turn to consider initial-boundary value problems. It is the Prandtl–Meyer flow with a turning angle of 10° at the body surface. The free stream state is $p = 1$, $\rho = 1$, and $M = 10$.

Both real and perfect gases are computed for comparison.

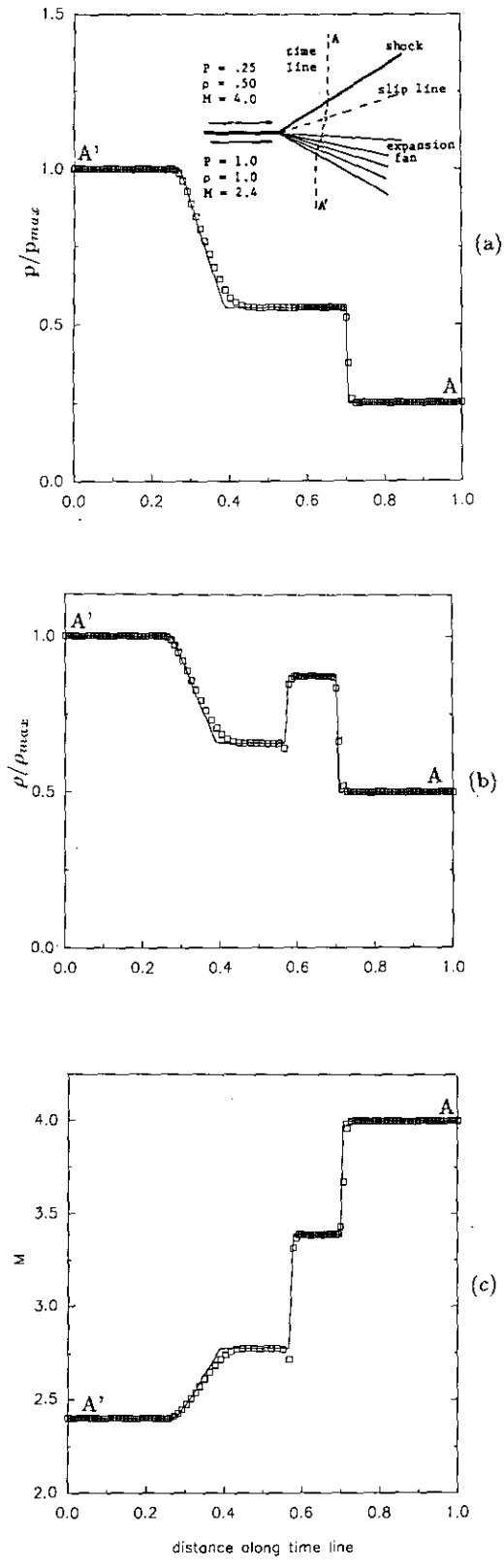

FIG. 4. Computational of perfect gas Riemann problem using real gas code: (a)–(c), flow variables along a typical time line; (a) pressure, (b) density, and (c) Mach number. Solid lines denote exact solutions.

In this problem 22 nonuniform cells are used, with cell size growing exponentially:

$$h_1 = 0.01;$$
$$h_j = 1.15 h_{j-1}, \qquad j = 2, 3, \ldots, 22.$$

Figure 5 illustrates the numerical results by the real gas code developed in the present paper and by the perfect gas code. For comparison the exact solution is also included. This problem is another low temperature case and the numerical results are practically identical; both agree very well with the exact solution. As a matter of fact, the numerical results arising from different codes are different only at the fifth decimal place.

In the next example, we still consider a Prandtl–Meyer expansion. However, the temperature is much higher so that the real gas effect is significant. We intend to show the numerical results with and without real gas effect. In this case the turning angle of the body surface is 20° and the free stream data reads:

$$p_\infty = 2, \qquad \rho_\infty = 0.25,$$
$$u_\infty = 15, \qquad v_\infty = 0.$$

Again 22 nonuniform cells are employed, with cell size growing exponentially:

$$h_1 = 0.01;$$
$$h_j = 1.075 h_{j-1}, \qquad j = 2, 3, \ldots, 22.$$

With the same free stream data, numerical computations using real gas and perfect gas EOSs respectively are carried out. Their results at $\tau = 0.12$ are illustrated in Fig. 6. For comparison, exact solutions are also included. It is observed with exactly the same initial data; there are differences due to the real gas effect in the computed pressures, densities, and, in particular, temperatures.

In the fourth example, we investigate oblique shocks and their interaction. First, two shocks are generated on both the upper and lower walls at the inlet of a converging channel. Then the shocks collide with each other and produce two new shocks and a slip line between them. The upper and the lower wall wedge angles are 10° and 20°, respectively. The flow variables of the oncoming free stream are

$$p = 2, \qquad \rho = 1, \qquad u = 13.1483, \qquad v = 0.$$

The same initial data is used for real gas computation and perfect gas computation. In both computations, 50 uniform cells with $h_j = 0.01$ are employed. Special treatments at the sudden body turns as described in [13] are applied to

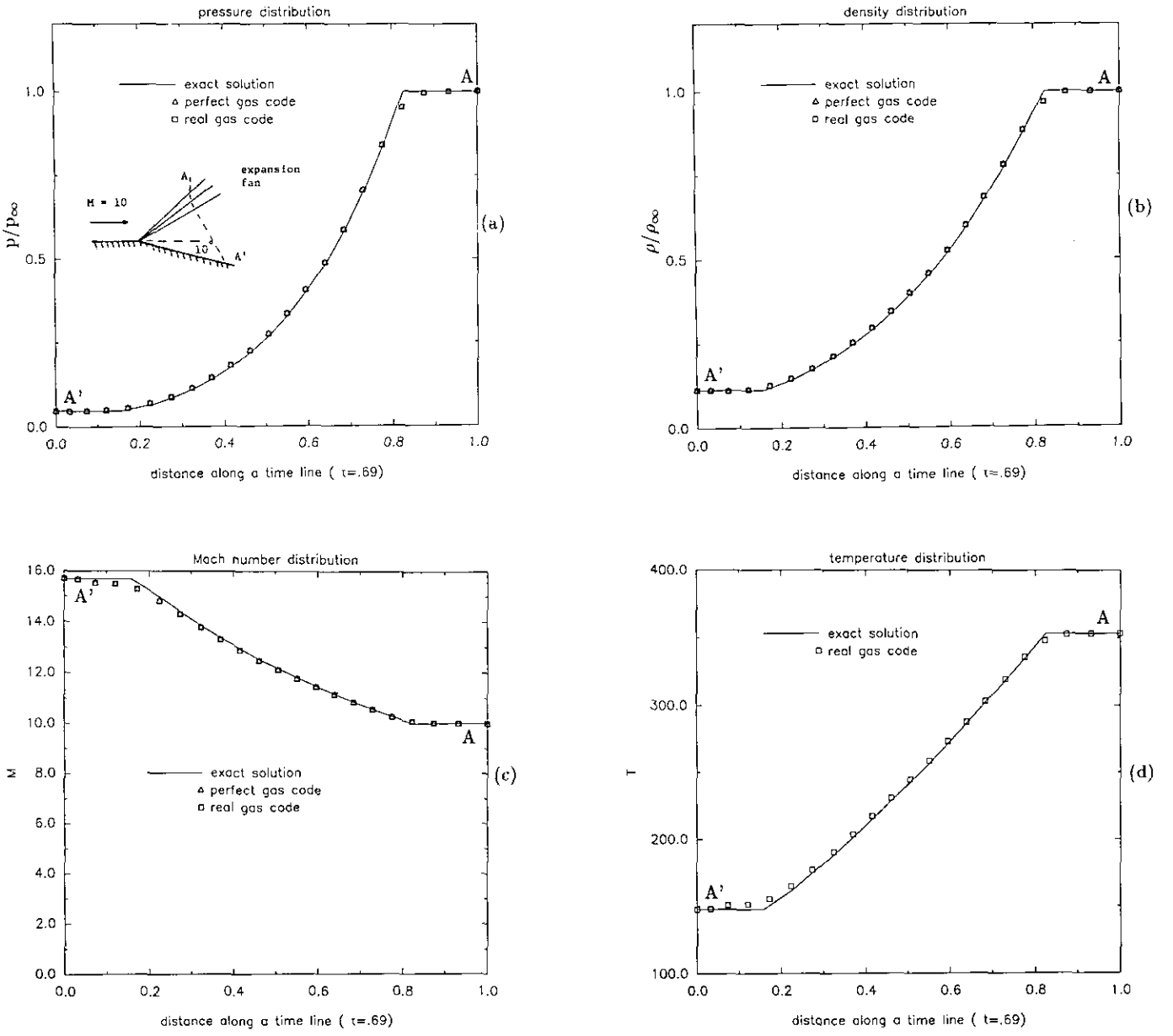

FIG. 5. Computational of a perfect gas Prandtl–Meyer flow using both perfect gas code and real gas code, showing the agreement of the numerical results: (a) pressure; (b) density; (c) Mach number; (d) temperature calculated by real gas code along a typical time line.

reduce the local numerical errors. Figures 7a and b illustrate the pressure and density along a typical time line after shock collision in the real gas case ($M = 8$), along with the exact solutions (solid lines). The numerical results agree well with the exact ones; the shocks are seen to be resolved in two points and the slip line in one point. Figures 8a, b, and c are the pressure, density, and temperature contours for the real gas flow. For comparison, the pressure and density contours for perfect gas are presented in Figs. 9a and b. It is observed that real gas shock collision takes place slightly later than its perfect gas counterpart.

The last example presents a more sophisticated problem which is a simulation of a supersonic jet engine outlet. Two streams are separated by a solid plate and then at $\tau = 0$ they begin to interact. The flow variables for the top stream and the bottom stream are respectively

$$p = 1, \qquad \rho = 0.1, \qquad u = 20, \qquad v = 0$$

and

$$p = 0.125, \qquad \rho = 0.0125, \qquad u = 22.5, \qquad v = 0.$$

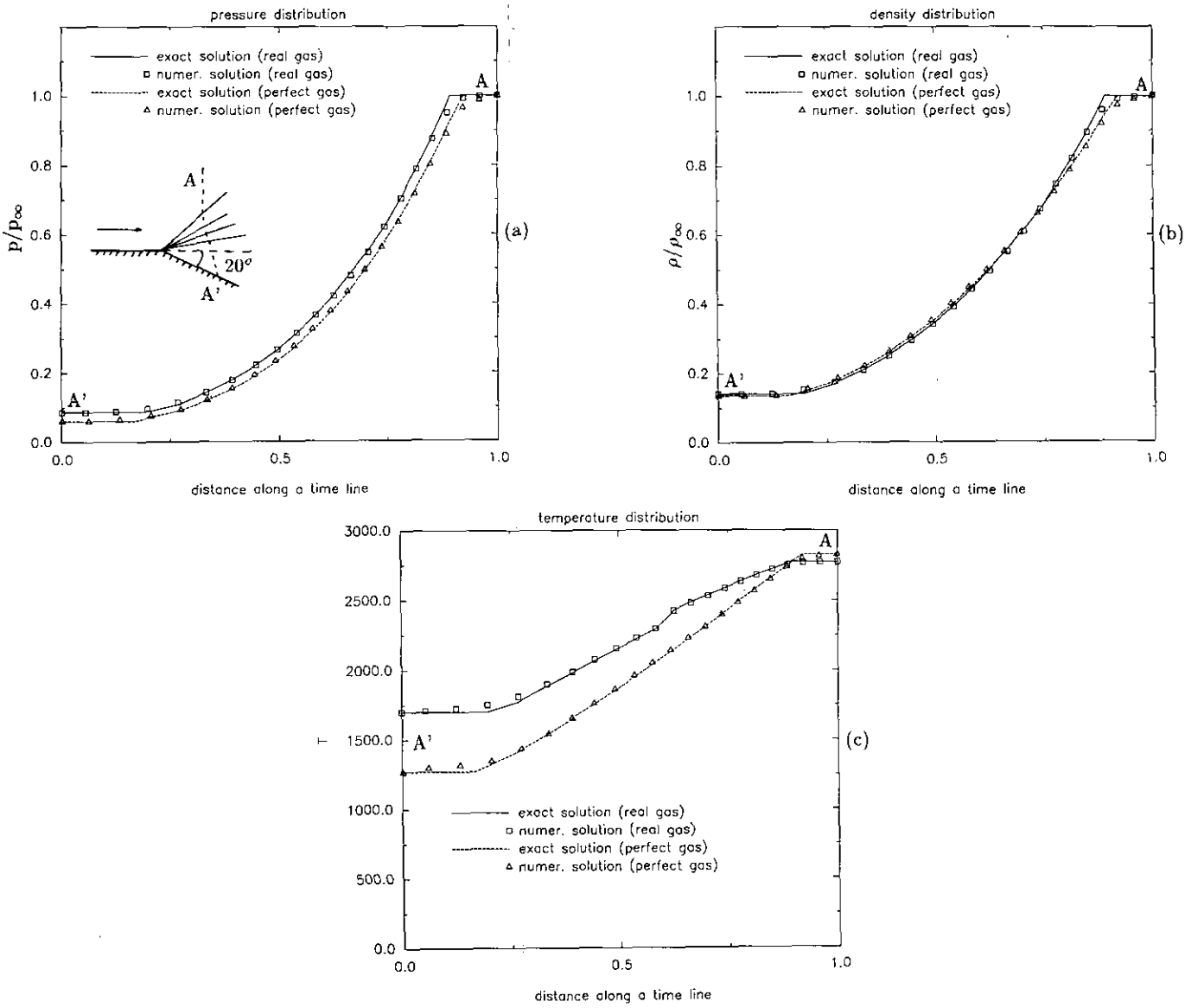

FIG. 6. Computation of a real gas Prandtl–Meyer flow using both perfect gas code and real gas code, showing the differences in the numerical results: (a) pressure; (b) density; (c) temperature along a typical time line.

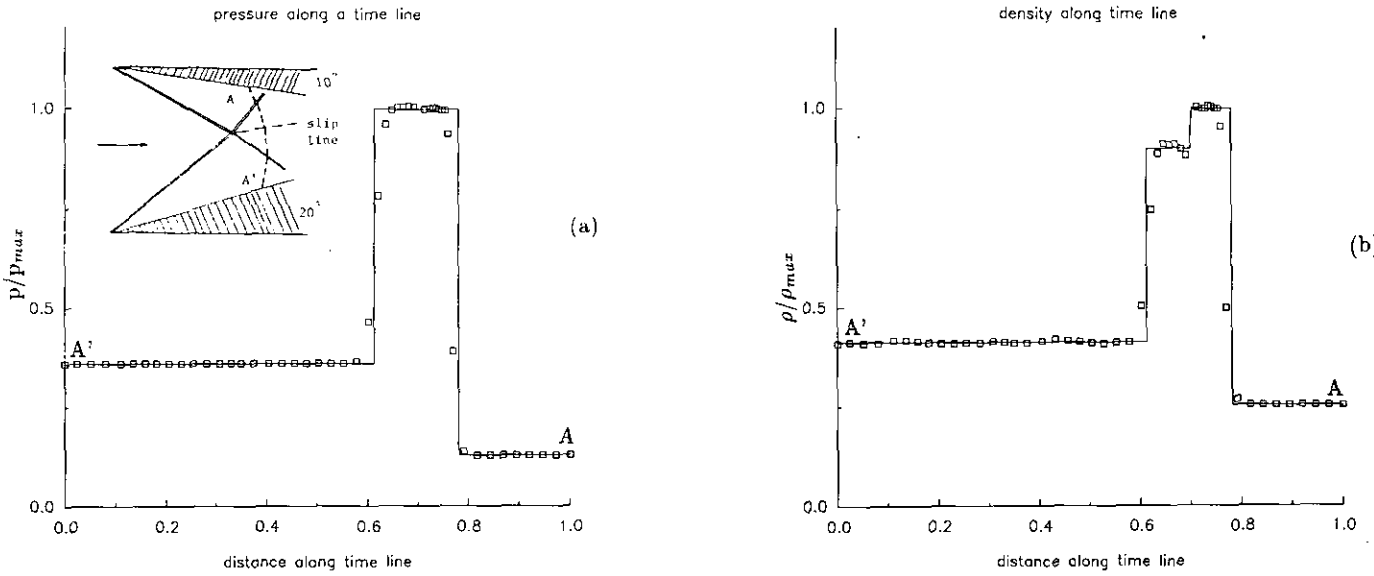

FIG. 7. Flow variables along a typical time line after shock–shock interaction in the real gas channel problem: (a) pressure and (b) density. Solid lines denote exact solutions.

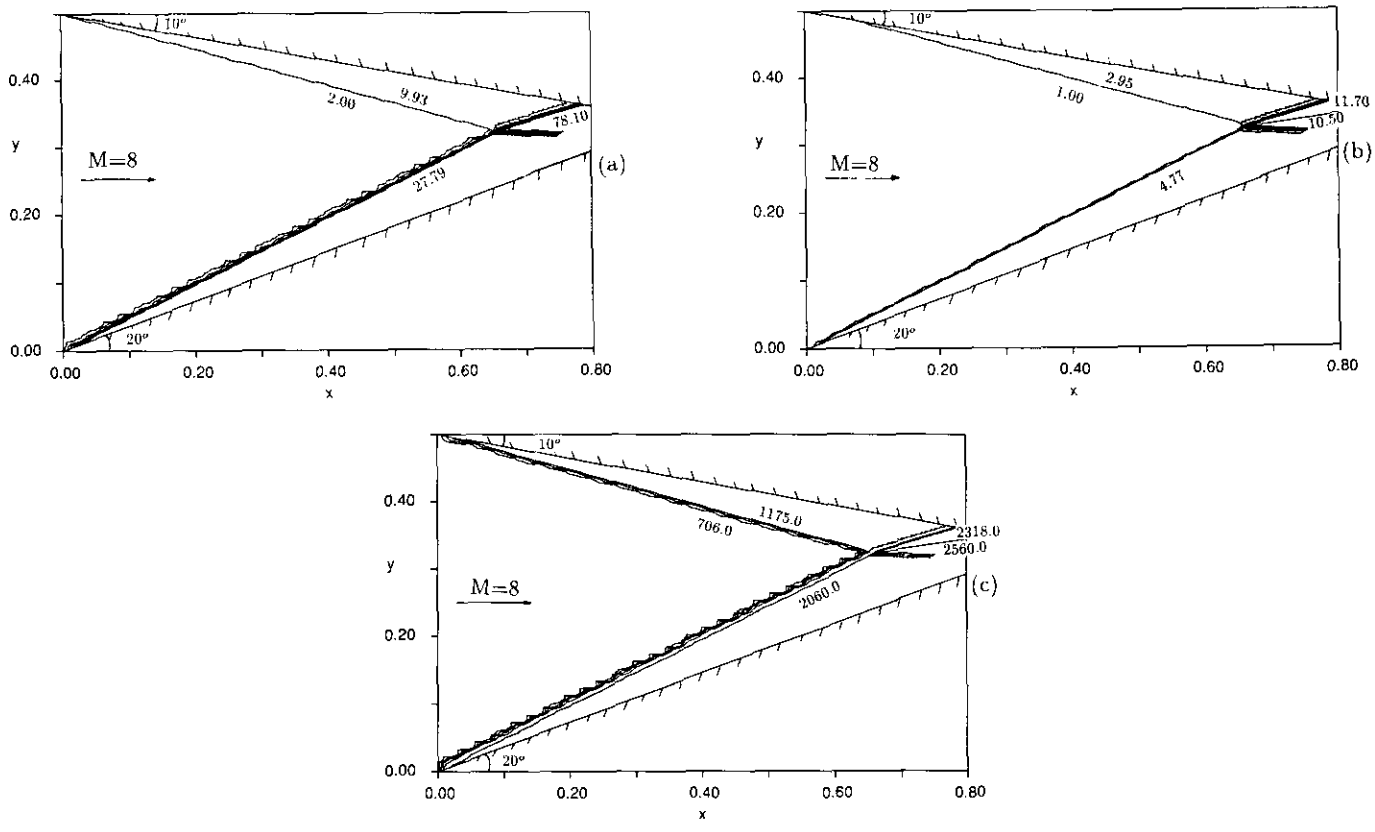

FIG. 8. Pressure, density, and temperature contours for the real gas channel problem: (a) isobars; (b) isopycnics; (c) isotherms.

The solid body surface under the bottom stream bears a sudden expansion turn of 5° and then extends as a straight line. The solid plate separating the two streams protrudes slightly in the forward direction. The interaction of the two streams produces a shock, a slip line, and an expansion fan. In addition, another expansion fan is issued from the sudden turn at the body surface. Subsequently, these waves interact with one another. The oblique shock bends as it goes through the interaction with the lower expansion fan and then reflects at the body surface. The reflected shock is hit by the strong slip line and deflected. In the meantime, the slip line itself is deflected by the collision and a narrow expansion fan is produced as well. The flow pattern is sketched in Fig. 10a and in Figs. 10b, c, and d we show the isobars, isopycnics (constant density), and isotherms, respectively. From Fig. 10b one observes the shock issued, reflected at the body surface, and deflected at the intersect with the slip line; on the other hand, the lower expansion fan

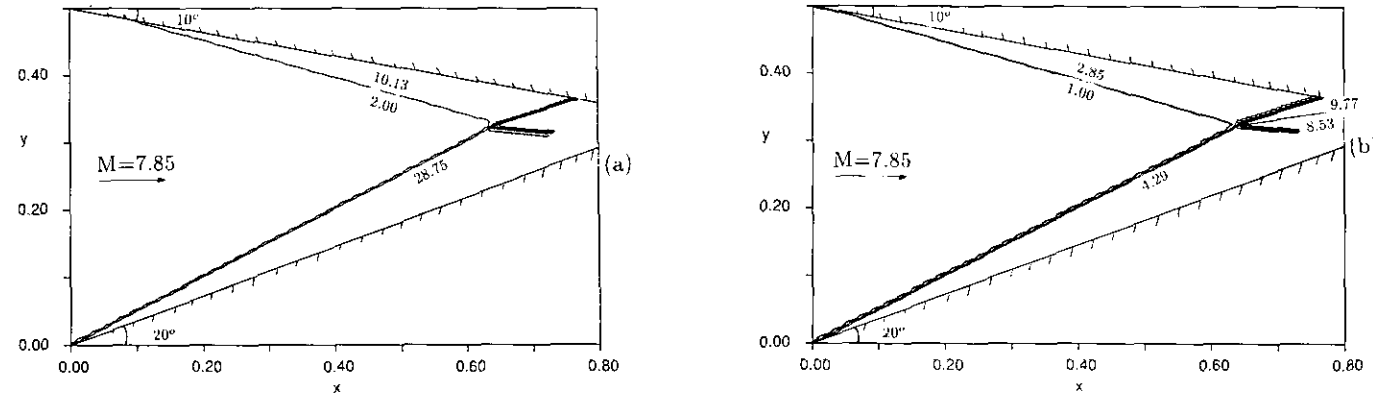

FIG. 9. Pressure and density contours for the perfect gas channel problem using the same initial data as the real gas: (a) isobars and (b) isopycnics.

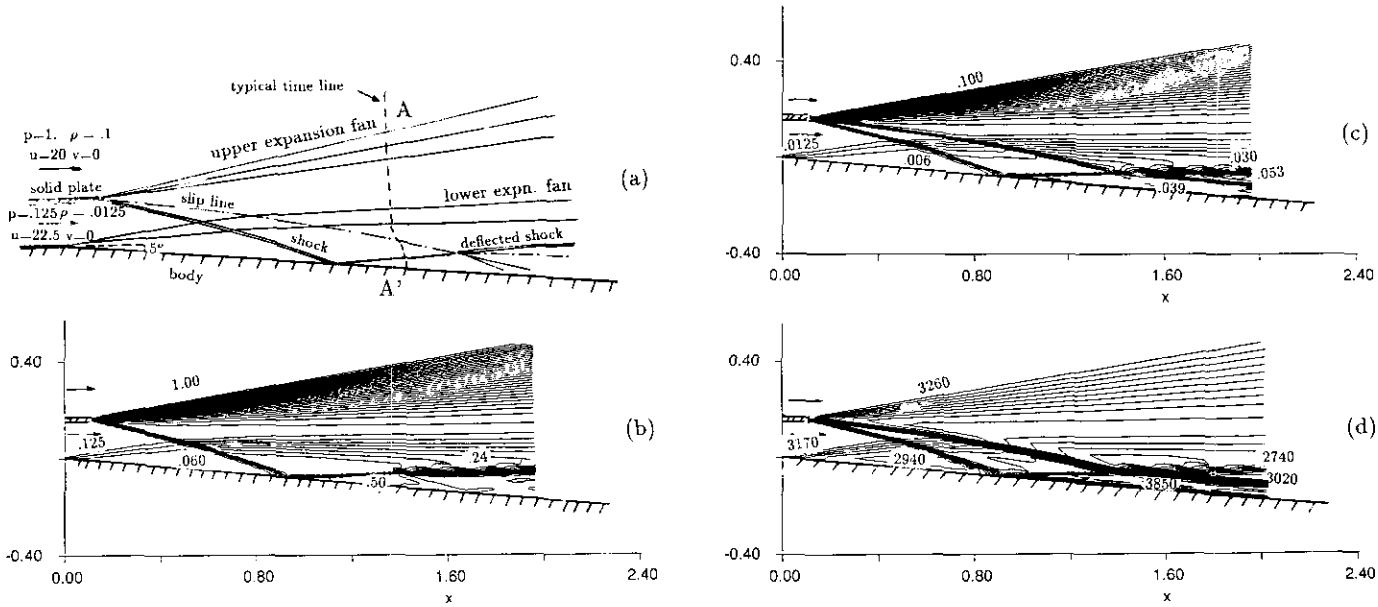

FIG. 10. Pressure, density, and temperature contours for a real gas outlet problem, showing interactions among the waves and shock reflection on the body surface: (a) schematic sketch; (b) isobars; (c) isopycnics; (d) isotherms.

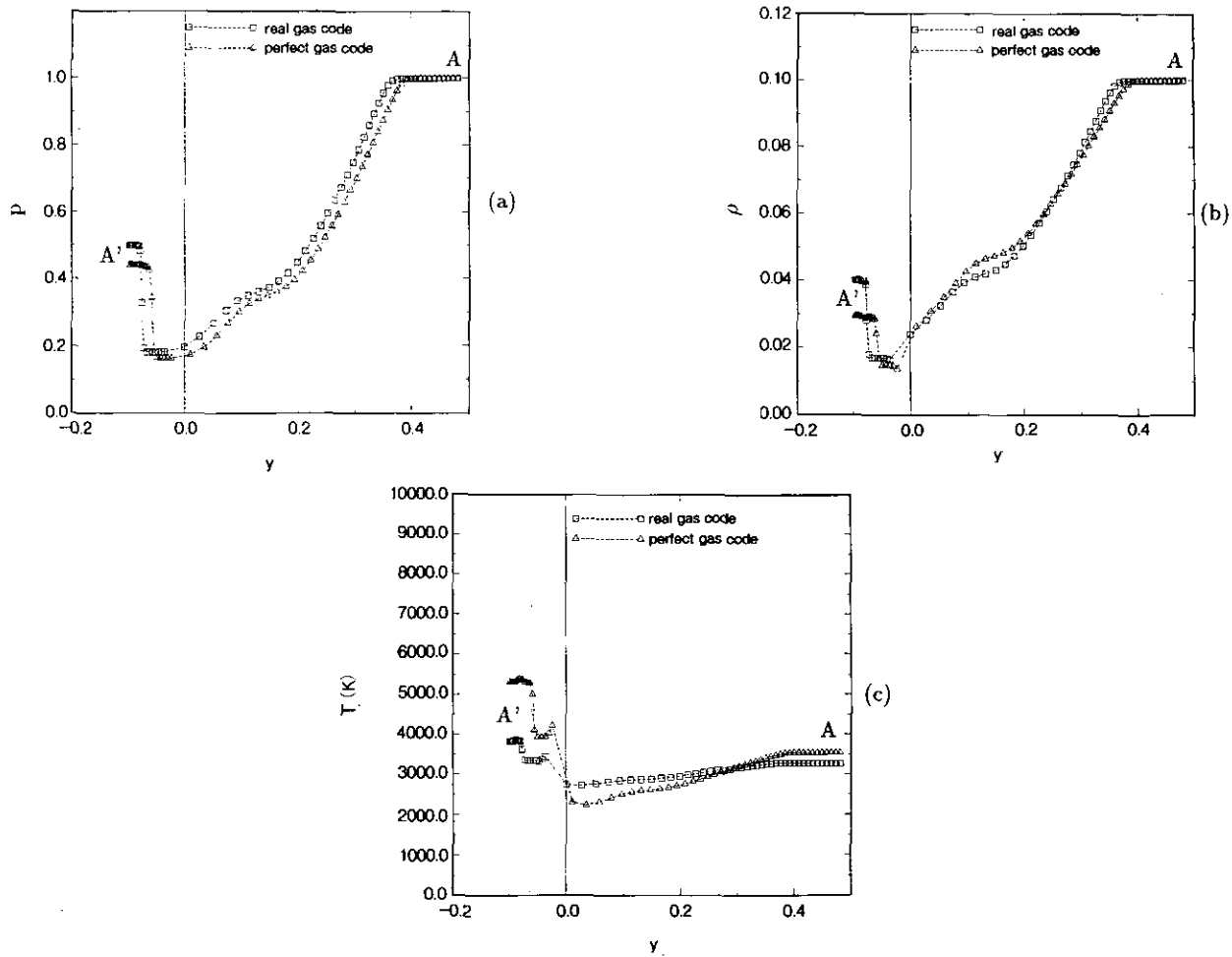

FIG. 11. Comparison of the numerical results from real gas code and perfect gas code for the outlet problem, showing flow variables along a typical time line: (a) pressure; (b) density; (c) temperature.

is seen deflected when passing through the shock and the slip line. In Fig. 10c the slip line is clearly shown and is seen deflected after impinging with the reflected shock.

For comparison, the same initial data is used to compute a perfect gas flow over the same body surface. As in the previous example of shock collision, the oblique shock in the perfect gas case hits the body surface slightly earlier (not shown). Figure 11 shows the more pronounced differences between the real gas and perfect gas results for the profiles of pressures, densities, and temperatures along a typical time line A'–A (shown in Fig. 10). Again, the computed shock and slipline are resolved in one to two cells.

In both computations, 60 uniform cells with $h = 0.01$ are used in order to cover the flow field we have shown; the upper 40 cells denote the top stream and the lower 20 cells denote the bottom stream. The initial time line bears an inclination angle of 54° which assures the stability in the time-marching process. Such a numerical stability problem involves a basic principle of wellposedness that the time line of a cell must lie outside the fan-shaped domains of influence issuing from its upper and lower cell interfaces. Details have been described by Hui and Loh [14].

5. CONCLUDING REMARKS

We have described the detailed formulation and the solution procedure for the Lagrangian conservative equations of real gases. The calculations demonstrated the accuracy of the Lagrangian approach over the Eulerian approach in handling oblique discontinuities. In particular, the slip line is resolved in at most two cells. The inherent parallelism, by following streamlines in the Lagrangian approach, also lends itself to the parallel computation. Recent results demonstrated significant gain in efficiency for the Lagrangian approach on the Connection Machine computer (CM-2) for both perfect and real gases [15, 16]. The 3D extension, as in the case of the 2D Eulerian approach, is not all that straightforward if a genuine multidimensional Riemann solver is demanded. However, allowing some degrees of approximation can make this extension feasible in practice. This work is currently underway.

REFERENCES

1. S. K. Godunov, *Mat. Sb.* **47**, 357 (1959).
2. S. Osher and F. Solomon, *Math. Comput.* **38**, 339 (1982).
3. P. L. Roe, *J. Comput. Phys.* **43**, 357 (1981).
4. B. van Leer, *SIAM J. Sci. Stat. Comput.* **5**, 1 (1981).
5. J. L. Steger and R. F. Warming, *J. Comput. Phys.* **40**, 395 (1981).
6. W. Hermann and L. D. Bertholf, in *Computational Methods for Transient Analysis*, edited by T. Belytschko and T. J. R. Hughes (North-Holland, Amsterdam, 1983), Chap. 8.
7. C. Y. Loh and W. H. Hui, *J. Comput Phys.* **89**, 207 (1990).
8. M.-S. Liou, B. van Leer, and J. S. Shuen, *J. Comput. Phys.* **87**, 1 (1990).
9. A. Suresh and M.-S. Liou, *Int. J. Numer. Methods in Fluids*, to appear.
10. W. H. Hui and H. van Roessel, in *Proceedings, NATO AGARD Symposium on Unsteady Aerodynamics—Fundamentals and Application to Aircraft Dynamics, Göttingen, West Germany, 1985*, S1, CP-386.
11. J. C. Tannehill and P. H. Mugge, NASA CR 2470, 1974 (unpublished).
12. P. K. Sweby, *SIAM J. Numer. Anal.* **21**, 995 (1984).
13. W. H. Hui and C. Y. Loh, *J. Comput. Phys.* **103**, 450 (1992).
14. W. H. Hui and C. Y. Loh, *J. Comput. Phys.* **103**, 465 (1992).
15. M.-F. Liou and C. Y. Loh, NASA TM-104446, 1991; in *Proceedings, Parallel Comput. Fluid Dynamics, Stuggart, Germany*, **1991**, edited by K. G. Reinsch *et al.*
16. M.-F. Liou and C. Y. Loh, NASA TM, to appear.